Two Balzan Research Projects

Federico Capasso

2016 Balzan Prize for Applied Photonics

Balzan GPC Adviser: Carlo Wyss
Project Supervisor: Federico Capasso
Researchers: Project 1: Miriam Serena Vitiello; Project 2: Margherita Maiuri
Affiliated Institutions: Project 1: Harvard School of Engineering and Applied Sciences, Harvard University, Cambridge MA; Project 2: Princeton University, Princeton, NJ; Polytechnic University of Milan
Period: 2017-

Federico Capasso is Robert Wallace Professor of Applied Physics and Vinton Hayes Senior Research Fellow in Electrical Engineering, Harvard School of Engineering and Applied Science, Cambridge, Massachusetts.

Two research projects have been undertaken by Federico Capasso's young researchers:

1. Optoelectronics and nano-photonics in two-dimensional nanomaterial hetero-structures;
2. Quantum Effects in Complex Systems ('Q-EX').

Project 1: Optoelectronics and nano-photonics in two-dimensional nanomaterial heterostructures

Institution: Harvard School of Engineering and Applied Sciences, Harvard University, Cambridge MA
Supervisor: Prof. Federico Capasso
Proposed beneficiary: Dr. Miriam Serena Vitiello (CNR NANO - Nanoscience Institute, National Enterprise for Nanoscience and Nanotechnology (NEST), Scuola Normale Superiore, Pisa)

Summary of achieved results

1. Tracing terahertz plasmon polaritons with a tunable-by-design dispersion in topological insulator metaelements

Collective oscillations of massless charge carriers in two-dimensional materials—Dirac plasmon polaritons (DPPs)—are of paramount importance for engineering nanophotonic devices with tunable optical response. However, tailoring the optical properties of DPPs in a nanomaterial is a very challenging task, particularly at terahertz (THz) frequencies, where the DPP momentum is more than one order of magnitude larger than that of the free-space photons, and DDP attenuation is high. The team conceive and demonstrate a strategy to tune the DPP dispersion in topological insulator metamaterials. The team engineer laterally coupled linear metaelements, fabricated from epitaxial Bi2Se3, with selected coupling distances with the purpose to tune their wavevector, by geometry. The team launch and directly map the propagation of DPPs confined within coupled meta-atoms via phase-sensitive scattering-type scanning near-field nanoscopy. The team demonstrate that the DPP wavelength can be tuned by varying the metaelements coupling distance, resulting in up to a 20% increase of the polariton wavevector Re(k_p) in dimers and triplets with a 1 μm spacing, with reduced losses and a >50% increase of the polariton attenuation length.

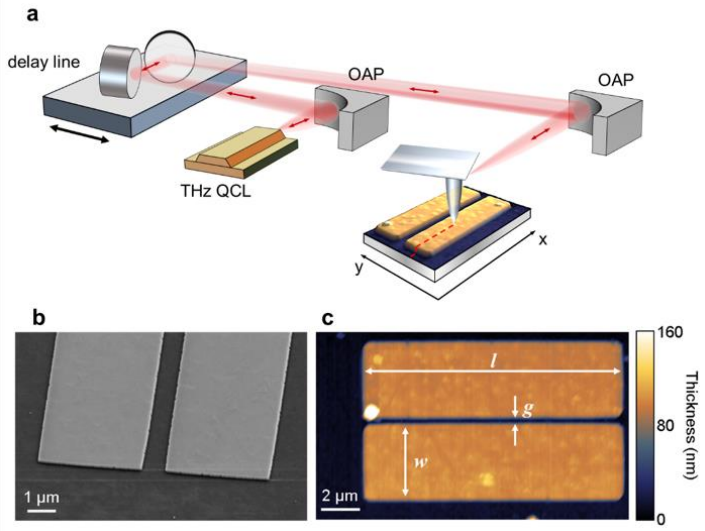

Figure 1. (a) Schematic of the THz s-SNOM setup in detector-less configuration. The output THz radiation from the QCL is collimated by an off-axis parabolic (OAP) mirror. The optical path length is set by a delay line. The AFM tip tapping frequency is Ω~53 kHz. SM signal is measured with a lock-in amplifier as a modulation of the voltage across the QCL terminals. A full description of the setup is given in the Methods section. **(b)**30° tilted SEM image of one of the fabricated Bi_2Se_3 resonators on a sapphire (Al_2O_3) substrate. **(c)** AFM image of a 16×4 μm^2 dimer with 0.5 μm gap. Italic letters *l*, *w*, and *g* indicate the length, width and gap of the coupled resonators, respectively. A full description of the fabrication procedure is given in the Supplementary Information.

The adopted THz s-SNOM apparatus, operates in a phase-sensitive detectorless configuration through self-mixing (SM) interferometry with a set of three THz QCLs. This method has proven instrumental for launching and capturing the propagation of THz plasmon polaritons in samples with reduced dimensionality, via the real-space mapping of surface excitations with spatial resolution better than $\lambda_0/100$ where λ_0 is the wavelength of the free-space propagating wave. The laser beam is focused on an atomic force microscope (AFM) tip, which acts as a local plasmon excitation source when it is positioned above the sample surface. The illuminated tip induces a strongly confined polarization in the surface, and thus it can couple the incident beam to a surface-guided polariton with a wavevector much higher than that of the free-space propagating wave. In our Bi_2Se_3 resonators, the polariton travels along the antenna, reflects from the antenna ends back towards the AFM tip, which then scatters it back to the QCL. The scattered wave couples into the laser cavity and mixes with the field inside the cavity, resulting in a change of the QCL terminal voltage. For a tip tapping near the sample surface (~200 nm distance) with a frequency Ω, the terminal voltage therefore displays oscillation at the fundamental frequency and at higher harmonics (nΩ), enabling detection of extremely weak scattered waves without a THz detector.

This modulation of the QCL voltage, *i.e.* the near-field SM signal, carries information about the amplitude and phase of the launched DPPs, detectable even at the 5th harmonic frequency. The phase is extracted readily by varying the optical path length L between the QCL and the AFM tip, by means of an optical delay line, and recoding an interferometric pattern. The adopted SM detection scheme is inherently fast due to the picosecond lifetime of carriers in QCLs. Therefore, by varying L with a constant velocity during the acquisition of a two-dimensional (x,y) s-SNOM image, it is possible to reconstruct an optical hologram $H_n(x,y) = A_n(x,y) \times \exp(iP_n(x,y))$, enabling phase ($\phi_n$) and amplitude ($s_n$) 2D near-field imaging at the nth order harmonic $\tilde{\sigma}_n(x,y) = s_n(x,y) \times \exp(i\phi_n(x,y))$ by means of post-processing.

The devised rectangular antennas were designed to be approximately twice as long as the expected DPPs wavelength at 3 THz. For this antenna length, tip-launched DPPs produce at least two full oscillations of SM phase signal ϕ_n along the antenna sufficient to determine the k-vector. The fabricated antennas are 16 μm long (l) and 4 μm wide (w). These were etched from an 80 nm thick continuous film of MBE-grown Bi_2Se_3 on sapphire Scanning electron microscope (SEM) images and AFM topography of the fabricated coupled resonators are shown in **Figure 1b,c-** The rectangular antenna geometry, with one dimension much shorter than the other, allows us to confine the polariton propagation to a single dimension, avoiding the geometrical decay caused by the radial divergence of tip-launched waves.

From the analysis of the collected phase oscillations the team obtained the complex-value of the plasmon-polariton wavevector $k_p = \mathrm{Re}(k_p) + i\mathrm{Im}(k_p)$, which encodes the polariton propagation characteristics, in particular the polariton wavelength $\lambda_p = 2\pi/\mathrm{Re}(k_p)$ and its damping length $L_p = 1/\mathrm{Im}(k_p)$. The results of the analysis are shown in **Figures 2**, which display the extracted dispersion (**Figure 2a-c**) and damping (**Figure 2d-f**) retrieved for all the measured coupled resonator configurations, at the three frequencies under study: 3.0 THz, 3.4 THz and 4.3 THz, indicated as dashed horizontal lines (Figures 4b,c). **Figure 2a** displays the measured DPP dispersion for a standalone 16 μm × 4 μm resonator, demonstrating a wavelength compression ratio (λ_0/λ_p) ~10, consistent with previous reports. The experimental data are compared to the polariton dispersion predicted by an analytical conductivity model. In this model, the Bi_2Se_3 layer is considered as a

layer of zero thickness, with a total conductivity (σ_t) given by the sum of bulk (σ_{bulk}), massive surface carriers (σ_{2DEG}), and Dirac carriers contributions (σ_{DC}). The complex polariton wave-vector k_p is evaluated as $k_p = ik_0\varepsilon_r \times (c/2\pi\sigma_t)$, where k_0 is the free-space wavevector, $\varepsilon_r = (\varepsilon_{sub} + \varepsilon_{sup})/2$ is the average permittivity of the materials surrounding the Bi_2Se_3 layer, and c is the speed of light. The best agreement between the experimental data points and the analytical model is achieved with the following values of carrier densities: $n_{bulk} = 1.8\times10^{19}$ cm^{-3}, $n_{DC} = 1.0\times10^{13}$ cm^{-2}, and $n_{2DEG} = 0.4\times10^{13}$ cm^{-2}, in good agreement with previous reports on similar structures.

The team also investigate how the dispersion of DPPs is modified when the Bi_2Se_3 antennas are laterally coupled in dimers or triplets. **Figures 2b,c** display the obtained results, indicating that the DPP's dispersion is notably different when the resonators are separated by a gap $g = 0.8$ µm. Specifically, the polariton wavevector Re(k_p) is increased by over 20% in dimers and triplets with this gap, compared to the predicted trend (dashed lines in Figures 4b,c) and to the case of standalone resonators. Interestingly, the coupling strength η, quantified here as the percentage increase of Re(k_p) relative to the standalone resonator, exhibits a non-monotonic dependence on the gap g between the two coupled resonators: η has a maximum value for $g = 0.8$ µm. This observation was attributed to the fact that, for $g = 0.3$ µm, the separation between two neighbouring antennas is small enough that the SPP is transmitted through the gap with negligible reflection.

The effect of lateral coupling can also be observed in the analysis of the DPP propagation length L_p. **Figure 2d** presents the Im(k_p) values plotted against Re(k_p) for all QCL frequencies for the standalone resonator. In this configuration, the ratio Re(k_p)/(2π×Im(k_p)) = L_p/λ_p, which represents the relative attenuation length of the SPP, remains almost constant regardless of frequency at approximately 0.36.

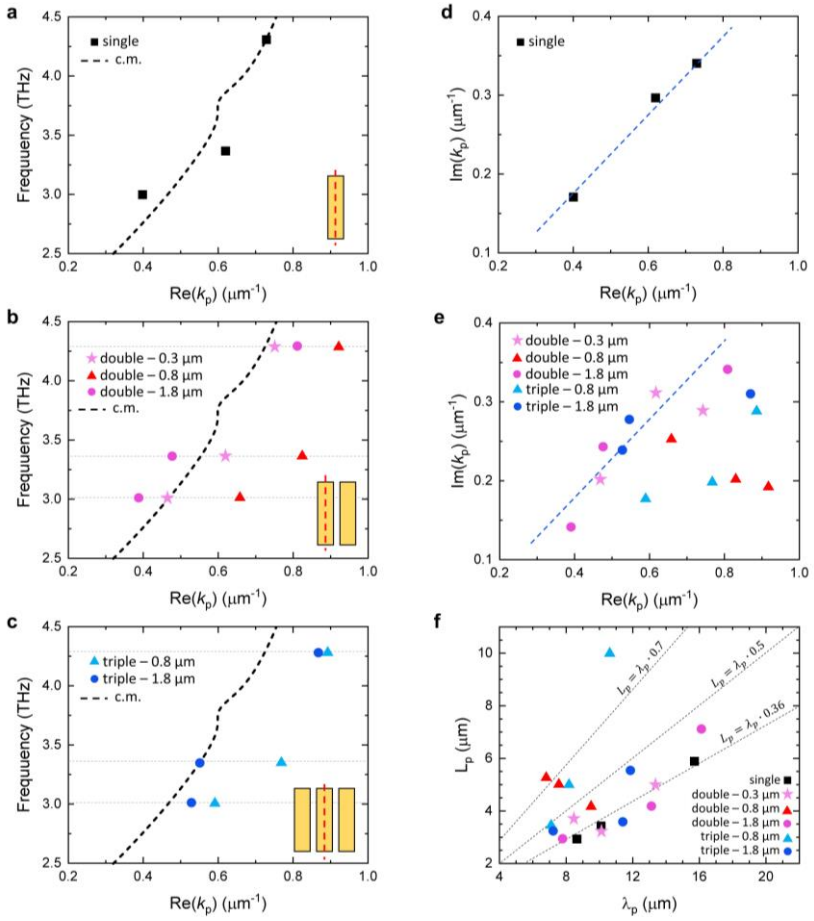

Figure 2. (a) Polariton dispersion obtained by fitting the experimental phase profiles for the single antenna. The black dashed line corresponds to the SPP dispersion predicted by an analytical conductivity model (c.m.), described in the Supporting Information. **(b,c)** Polariton dispersion for the doublet (b) and triplet (c) configurations. The black dashed lines correspond to the lines in (a), facilitating a direct comparison with the single antenna case. Horizontal lines indicate the three investigated frequencies: 3.0 THz, 3.4 THz and 4.3 THz. **(d)** Imaginary part *vs*. real part of the polariton wavevector for a standalone resonator. The blue dashed line is a guide to the eye. **(e)** Imaginary part *vs*. real part of the polariton wavevector in the cases of doublets and triplets. Dashed lines correspond to those in (d). **(f)** Polariton decay length (L_p) as a function of the polariton wavelength (λ_p). The dashed lines represent different proportional relationships between the two quantities. The line $L_p = \lambda_p \times 0.36$ is derived from a fit to the single-resonator measurements.

This value is consistent with that reported in previous studies on MBE-grown Bi_2Se_3 thin films and can be attributed to a smaller wavelength compression ratio λ_0/λ_p compared to other material systems, such as hBN-encapsulated graphene. Interestingly, the relative attenuation length is significantly improved in efficiently coupled resonators, as shown in **Figure 2e**, which plots Im(k_p) as a function of Re(k_p) for various configurations of coupled resonators. In this figure, data points to the right of the diagonal dashed line represent configurations with lower attenuation. This observation can be further clarified by visualizing the same results in the (L_p,λ_p) plane (see **Figure 2f**), where we observe that for a gap spacing of $g = 0.8$ µm and frequencies

above 3.4 THz, the relative attenuation length L_p/λ_p is approximately doubled with respect to that of the standalone antenna, indicating that the propagation losses are strongly reduced in laterally coupled systems. This loss reduction can be intuitively understood as a result of decreased lateral confinement of the propagating SPP along the antenna, due to the evanescent coupling with neighbouring structures. However, when the confinement is further reduced (g = 0.3 μm), the surface mode can spread across the separation gap, resulting in standard geometrical damping and cancelling out the benefits of the *quasi*-one-dimensional propagation. For larger gap spacing (g = 1.8 μm), the coupling between neighbouring resonators is strongly reduced, leading to propagation losses similar to that observed for the standalone antenna.

The investigation of tip-launched SPPs propagating at the TI surface shows that the gap (g) separation between adjacent resonators plays a crucial role in determining the polariton dispersion and dynamics. Importantly, g not only affects the wavelength but also influences the damping losses of the SPP modes excited on the TI surface. Our results demonstrate that it is possible to customize the spectral response of Bi_2Se_3-based THz resonators by adjusting the gap. This knowledge can be utilized as a design strategy for the implementation of TI-based architectures, taking advantage of various effects such as resonance line narrowing, resonance mode-splitting, and cross-polarization conversion, typically observed in coupled resonators systems. Additionally, we envision that lithographically designed THz metasurfaces using large-area TI materials with specific spectral responses can potentially have a significant impact on far-infrared optoelectronics and nonlinear nanophotonics.

Associated publications

1. L Viti, C Schiattarella, L Sichert, Z Wang, S Law, O Mitrofanov, MS Vitiello
   "Tracing terahertz plasmon polaritons with a tunable-by-design dispersion in topological insulator meta-elements", ***Nature Light Science&Applications*** 14, 288 (2025)

2. Mapping propagation of collective modes in Bi_2Se_3 and $Bi_2Te_{2.2}Se_{0.8}$ topological insulators by near-field terahertz nanoscopy

Near-field microscopy discloses a peculiar potential to explore novel quantum state of matter at the nanoscale, providing an intriguing playground to investigate, locally, carrier dynamics or propagation of photoexcited modes as plasmons, phonons, plasmon-polaritons or phonon-polaritons. The team exploited a combination of hyperspectral time domain spectroscopy nano-imaging and detectorless scattering near-field optical microscopy, at multiple terahertz frequencies, to explore the rich physics of layered topological insulators as Bi_2Se_3 and $Bi_2Te_{2.2}Se_{0.8}$, hyperbolic materials with topologically protected surface states. By mapping the near-field scattering signal from a set of thin flakes of Bi_2Se_3 and $Bi_2Te_{2.2}Se_{0.8}$ of various thicknesses, we shed light on the nature of the collective modes dominating their optical response in the 2-3 THz range. The team captured snapshots of the activation of transverse and longitudinal optical phonons and revealed the propagation of sub-diffractional hyperbolic phonon-polariton modes influenced by the Dirac plasmons arising from the topological surface states or bulk plasmons, prospecting new research directions in plasmonics, tailored nanophotonics, spintronics, and quantum technologies.

Flakes of thickness d in the range 15-200 nm and lateral size in the range 0.2-4 μm, are obtained by mechanical exfoliation on a 350 μm thick silicon wafer, with a 300 nm thin insulating SiO_2 top layer. The micro-Raman characterization[6] of a prototypical flake of Bi_2Se_3 and $Bi_2Te_{2.2}Se_{0.8}$ is reported in Supplementary figure S1a-b, respectively. Bi_2Se_3 and Bi_2Te_3 crystallize in tetradymites with rhombohedral crystal structure endowed with D^5_{3d} space group symmetry and five atoms per unit cell. The structure consists of quintuple layers (QL) stacked via weak van der Waals forces, which permit an easy mechanical exfoliation, orthogonally to the trigonal c-axis. One QL corresponds to a 1.42 nm thick crystal of Bi_2Se_3 and to 1 nm for $Bi_2Te_{2.2}Se_{0.8}$. Within each QL, pictogen (Bi) and chalcogen atoms (Se, Te) are held together by ionic covalent bonds. The different bond strength and character result into a strong in plane/out of plane anisotropy in the thermal, electronic, and dielectric properties of these materials.

With the aim of isolating the nature of the modes activated through THz induced photo-excitation and their interaction with TSS, the team then perform self-detection nanoscopy on a set of flakes with a progressively reduced thickness, employing single-frequency mode THz-QCLs, as sketched in Fig. 3a, operating at three different emission frequencies, ω_0 = 66.7 cm^{-1}, 76.7, 89.7 cm^{-1}, THz-QCLs have the inherent

advantage of providing mW output powers and high spectral purity, with intrinsic linewidths as low as 100 Hz; this allows for selective interaction with resonant modes.

The scattering signal at the highest harmonic order with $n = 5$, acquired keeping fixed the cavity length L, is enhanced at the flakes compared to the substrate, see Fig. 3d-e. For thicker flakes with $d > 40$ nm, the amplitude of s_5 appears higher for $Bi_2Te_{2.2}Se_{0.8}$ (B1-B2 in Fig. 3c) than for Bi_2Se_3 (A1-A2 in Fig. 3b) However, the two materials show a different dependence on thickness: while negligible amplitude variation is observed upon reducing the thickness for Bi_2Se_3 from 86 nm (flake A1) to 16 nm (A4) (see Fig. 3d), the s_5 amplitude drops in $Bi_2Te_{2.2}Se_{0.8}$ such that the 19 nm thick flake (B4) is barely distinguishable from the substrate (Fig. 3e).

The extracted line profiles from the maps in Fig. 3b-3e while moving along a line orthogonal to the flakes edge and keeping fixed the cavity length L, show the variation of the substrate/flake contrast with thickness in the two material systems (Fig. 3f-3g).

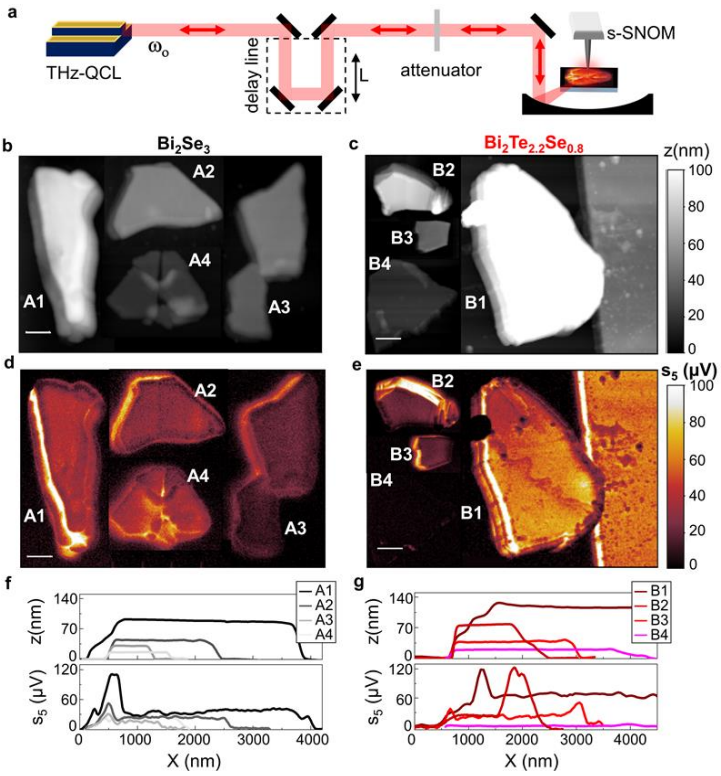

Figure 3: (a) Sketch of the self-detection nanoscopy experiment based on THz-QCL of frequency $\omega_0 = 66.7$, 76.7, 89.7 cm^{-1} simultaneously serving as source and detector of the backscattered field from the AFM tip of the s-SNOM with a delay-line controlling the length L of the optical path and an attenuator to reduce the feedback intensity; **(b-c)** topography maps of four distinctive flakes of Bi_2Se_3 (a) and $Bi_2Te_{2.2}Se_{0.8}$ (b) of variable thickness z with labels Ai and Bi, respectively, with $i = 1,2,3,4$. **(d-e)** Near-field fifth-order self-mixing signal s_5 maps of the flakes in panels (b-c) taken keeping a fixed external cavity length L measured with ω_0=66.7 cm^{-1} without attenuation. Scale bars in panels b-e correspond to 1 μm. **(f-g)** Line scans of the topography maps z and of the fifth-order self-mixing signal s_5 on four distinctive flakes of Bi_2Se_3 (f) and of $Bi_2Te_{2.2}Se_{0.8}$ (g), extracted from panels (b-c) and (d-e) while moving from substrate to the flakes along a line orthogonal to the flakes edge.

The thickness-dependent signal change, revealed in the maps (Fig. 3f-3g), could be caused by both a phase shift and by an actual variation of the amplitude of the self-mixing fringes. To discriminate between the two effects, the phase of the scattered field was resolved. The team acquired the self-mixing fringes with 0.2 μm steps, and we scan the sample along a line orthogonal to the substrate-flake edge. Fig. 4a shows the retrieved amplitude signal at the 3rd demodulation order s_3, as a function of L, and of the position on the sample, labeled as X.

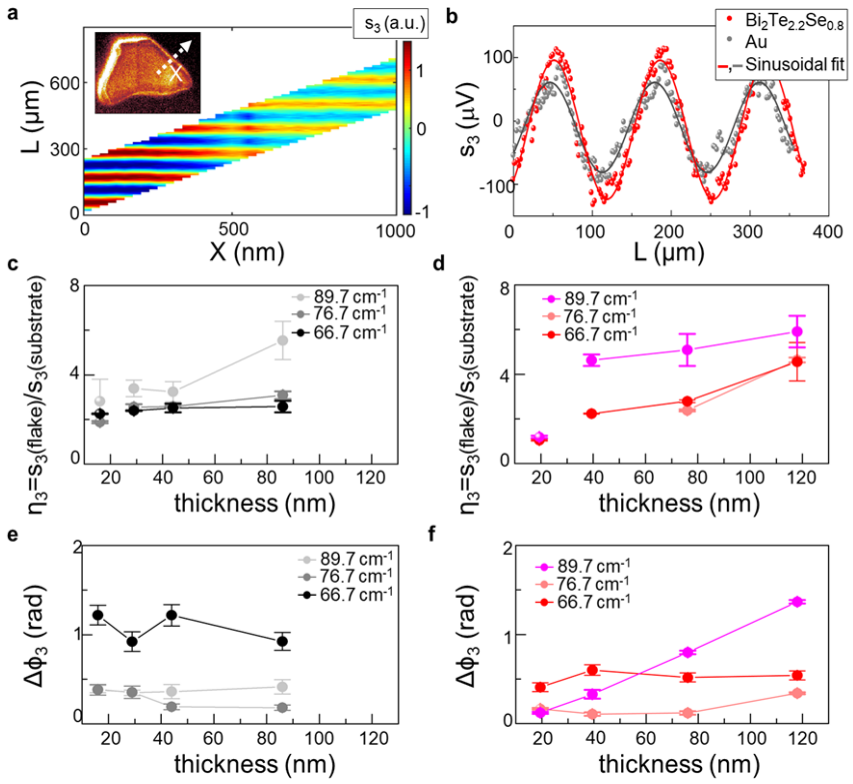

Figure 4: **(a)** SM maps of s_3 signal on flake A2 of Bi_2Se_3 as a function of the cavity length L and of the position X moving on a line orthogonal to the flake edge sketched in the inset by the white dashed arrow a s_3 map; the sampling interval changes with X due to the delay line backlash; **(b)** SM fringes of s_3 as a function of the cavity length L at a fixed position on flake B3 of $Bi_2Te_{2.2}Se_{0.8}$ (red dots) and the substrate (gray dots) acquired at 76.7 cm^{-1} together with sinusoidal best fit (solid lines); **(c-d)** Signal contrast η_3 evaluated dividing the signal amplitude s_3 on Bi_2Se_3 (c) and on $Bi_2Te_{2.2}Se_{0.8}$ (d) by that collected on the substrate, all extracted from the sinusoidal fit of the SM fringes acquired on 1 μm-length line scan across the flake/substrate interface, measured at three different probing frequencies; **(e-f)** Phase variation $\Delta\phi_3$ from the substrate to the flakes, extracted from the sinusoidal fit of the SM fringes acquired on 1 μm-length line scan across the flake/substrate interface, as a function of the flake thickness at the three different frequencies for Bi_2Se_3 (e) and $Bi_2Te_{2.2}Se_{0.8}$ (f).

Considering the drop in the scattering efficiency of the tip with increasing THz frequencies, we chose the third-order demodulated signal s_3 to compare the data collected at the three different frequencies ω_0. By analysing the self-mixing fringes at each X with sinusoidal fit functions (as in Fig. 4b), the team extracted the amplitude s_3 and the phase ϕ_3 along the scan trajectory. The thickness dependence of the ratio η_3, which is accounting for the contrast between flake and substrate, and of the phase change $\Delta\phi_3$, at the three pumping frequencies, are reported in Fig. 4c-4d and Fig. 4e-4f, respectively, for both Bi_2Se_3 and $Bi_2Te_{2.2}Se_{0.8}$ flakes. The near-field response appears very different in the two materials.

In Bi_2Se_3, the flat topography regions show roughly constant contrast with the SiO_2 substrate, at all the probing frequencies, while only the signal at the flake edges varies with the thickness. Looking to $s_3(\omega_0)$, by keeping fixed the layer thickness, the contrast η_3 increases by 30-40% while increasing ω_0 from ω_0= 66.7 cm^{-1} to ω_0= 76.7 cm^{-1} in Bi_2Se_3 (Fig. 4c). This is in disagreement with the calculated 2D near-field response of Bi_2Se_3 that predicts[31] a peak in the s_3 amplitude at the TO phonon wavenumber ω_{T0}= 65 cm^{-1} and a strong decrease of about 40% in the range 65 cm^{-1} – 90 cm^{-1}. On the other hand, the observed increase of s_3 is compatible with the overall increase in the same range shown by the calculated contrast in Fig.1e, and hence suggests a bulk phonon-like nature for the dielectric response of our Bi_2Se_3 samples. On the contrary, $Bi_2Te_{2.2}Se_{0.8}$ exhibits a visible decrease in the scattering intensity with flake thickness d at ω_0= 66.7 cm^{-1} and ω_0= 76.7 cm^{-1}, which becomes less pronounced at ω_0= 89.7 cm^{-1}, and becoming, in all cases, barely distinguishable (η_3~1) from the substrate when d <20nm (Fig. 3d). The thickness and frequency dependences of s_3 from $Bi_2Te_{2.2}Se_{0.8}$ are consistent with a recent model of the near-field response formulated for Bi_2Se_3 which predicts deeply sub-diffractional, highly directional hyperbolic phonon polaritons interacting with the electrons of the TSS. In particular, the experimental signal frequency dependence of $Bi_2Te_{2.2}Se_{0.8}$ is retrieved if one includes a red-shift of the spectral features predicted by the model for Bi_2Se_3 towards the optical phonon frequencies of the Bi_2Te_3 to describe $Bi_2Te_{2.2}Se_{0.8}$, whose phonon frequencies reasonably approaches the ones of Bi_2Te_3 Consistently, in the $Bi_2Te_{2.2}Se_{0.8}$ flakes (Fig. 4d) s_3 (ω_0) is almost frequency independent in the 66.7 cm^{-1} < ω_0 < 76.7 cm^{-1} range and then increases when ω_0 = 89.7 cm^{-1} as we approach the peak of s_3 due to $\omega_{//}$ = 95 cm^{-1}. A strong and sharp peak in near-field contrast is predicted at $\omega_{to}^{\perp}$, that in a $Bi_2Te_{2.2}Se_{0.8}$ falls outside of the investigated spectral range ($\omega_{to}^{\perp}$= 50 cm^{-1} for the Bi_2Te_3). However, differently from the peak at $\omega_{//}$, this peak is related to the far-field factor rather than to surface excitations.

Propagating collective excitations

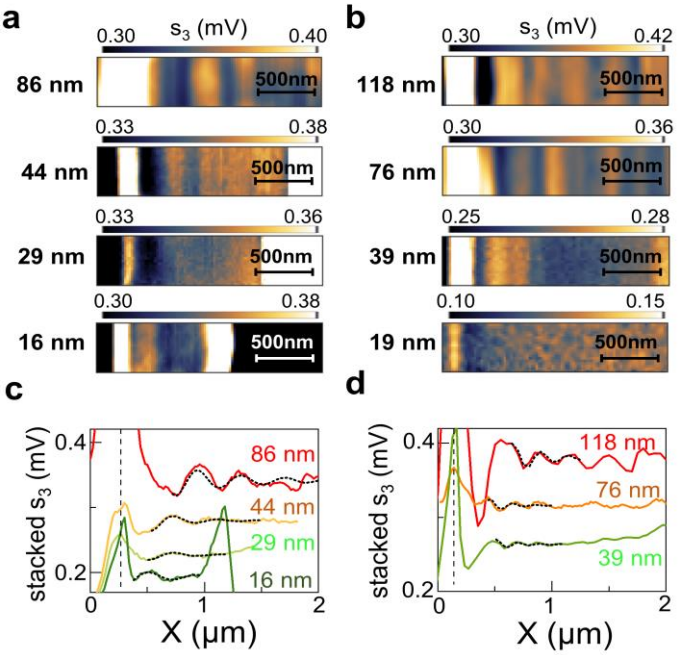

Figures 5 show the near-field maps (Fig.5a-5b) of the edges of the Bi_2Se_3 and $Bi_2Te_{2.2}Se_{0.8}$ flakes, acquired at 66.7 cm^{-1} for a fixed cavity length L, and the related line profiles extracted while averaging over the displayed window along the vertical axis (Fig.5c-5d).

Figure 5: (a-b) Near-field scattering maps of s_3 signal acquired at 66.7 cm^{-1} at the flakes edge of Bi_2Se_3 (a) and $Bi_2Te_{2.2}Se_{0.8}$ (b) with different thicknesses as indicated on the side. The scale bar corresponds to 500 nm; **(c-d)** Line-profiles (colored solid lines) extracted averaging the maps in panels a-b vertically on the displayed window, showing the signal oscillations as a function of the position X for flakes of Bi_2Se_3 (c) and $Bi_2Te_{2.2}Se_{0.8}$ (d). The line profile corresponding to the map of the 19 nm-thick flake of $Bi_2Te_{2.2}Se_{0.8}$ is not reported because it lacks evident periodicity. The line profiles are aligned to have the highest peak at the same position identified by the black dashed vertical line. Fits of the oscillations to extract the periodicity, performed with the function described in the text, are plotted as short-dot black lines.

The near-field scattering maps (Fig. 5a-5b) show a visible signal enhancement at the flake edges with the brightest edge always corresponding to the side from which the THz beam enters in the s-SNOM, independently on the scanning direction.

A strong signal enhancement at the flakes edges has been previously identified in hBN as a signature of activation of localized phonon-polariton modes. The peaks localized at the flake edges have distinct thickness dependence in the two materials: in the Bi_2Se_3 the peak broadens and increases its intensity with thickness (Fig.5c), while it appears always sharper, and with a less pronounced thickness dependent intensity in the $Bi_2Te_{2.2}Se_{0.8}$ (Fig. 5d). We ascribe those peaks to edge resonances of phonon-polariton modes, whose interplay with the main photoexcited modes quickly damp them close to the edge. Indeed, while the peaks retrieved in Fig. 5c and 5d are visibly edge modes, we observe signal intensity modulations in regions on flat topography (Fig.5c-5d) characterized by a much weaker amplitude, which we attribute to the interference of propagating modes launched by the tip and reflected at the flake edges. In the present case, these oscillations in Bi_2Se_3 have comparable amplitude changing the thickness, while in $Bi_2Te_{2.2}Se_{0.8}$ they display a less pronounced intensity for thinner flakes, becoming not distinguishable in the thinner flake (d = 19 nm).

To unveil the nature of the aforementioned photoexcited modes, the team analyzed these signal oscillations with the function: $s_3(x) = Re\left(\frac{A}{\sqrt{x-x_0}} e^{2iq_p(x-x_o)}\right) + B$, expected for modes launched by the tip and reflected by the flake edges[59]. In the fitting function A is a complex-valued amplitude, B is a constant background, x_0 represents the position of the reflecting interface taken as the flakes' edge (dashed line in Fig. 5c-d), $1/\sqrt{x-x_0}$ is the geometrical decay and the exponential describes oscillations with periodicity $\frac{4\pi}{q_p}$ where the wavevector q_p is complex-valued $q_p = q_1 + iq_2$. The double period $\lambda_p = \frac{2\pi}{q_1}$ represents the wavelength of the photoexcited modes, whose frequency is set by the energy conservation law to match that of the impinging photon.

Figure 6a shows the obtained λ_p as a function of the flake thickness for Bi_2Se_3 and $Bi_2Te_{2.2}Se_{0.8}$, respectively, at the three probed frequencies. In Bi_2Se_3, λ_p is almost thickness independent (Fig. 6a), at all probing frequencies. Vice versa, in $Bi_2Te_{2.2}Se_{0.8}$, there is a visible dependence of the oscillation period from d (Fig. 6b): λ_p decreases while reducing d.

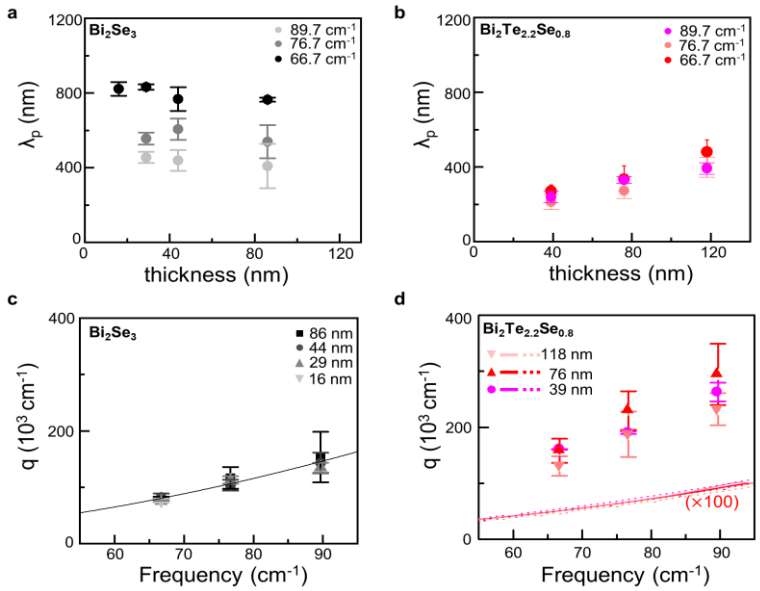

Figure 6: (a) Plasmon wavelength λ_p in Bi_2Se_3 as a function of thickness, extracted from the interference pattern measured at 66.7 cm^{-1} (black dots), at 76.7 cm^{-1} (gray dots) and 89.7 cm^{-1} (light gray dots). **(b)** Wavelength λ_p of the photo-excited modes in $Bi_2Te_{2.2}Se_{0.8}$ as a function of thickness extracted from the interference pattern measured at 66.7 cm^{-1} (red dots), at 76.7 cm^{-1} (light red dots) and 89.7 cm^{-1} (magenta dots). **(c)** Plasmon energy dispersion in Bi_2Se_3 for different thicknesses ranging from 86 nm to 16 nm (colored dots) together with the predicted dispersion law (solid line). **(d)** Energy dispersion of the photo-excited modes in $Bi_2Te_{2.2}Se_{0.8}$ for different thicknesses ranging from 118 to 39 nm (colored dots), compared to the energy dispersion simulated for Dirac plasmons (colored solid lines) and massive bulk plasmons (colored dot lines) reported in Fig.S12 (Supporting Information) and therein-discussed in detail.

The thickness-independent trend, extrapolated in Bi_2Se_3, is compatible with photoexcited massive plasmons formed by the bulk charge carriers at the flakes surface, which give rise to a 2DEG, as a consequence of the band bending at the Bi_2Se_3 interface with adjacent materials.

Conversely, the extrapolated thickness dependence of λ_p in $Bi_2Te_{2.2}Se_{0.8}$, is expected either in presence of both massive plasmons related to bulk charge carriers, or for Dirac plasmons related to TSS. It is worth mentioning that, in the limit of small wavevectors (qd<1), Dirac plasmons dispersion can be approximated to the thickness independent first order dispersion, while at larger wavevectors both the dependence on the thickness and on the bulk dielectric function emerge.

The team finally investigate the experimental mode dispersion (Figure 6c-6d), for both material systems and compare it with the theoretical trends predicted under the hypothesis discussed above. A quadratic dependence of the real part of the wavevector $q_1 = 2\pi/\lambda_p$ from the frequency $\omega_p = \omega_0$ is observed for both materials. In Bi_2Se_3 the dispersion curve, calculated for massive plasmons formed by the 2DEG charge carriers, perfectly matches our experimental data (Fig. 6c), confirming our claim. The dispersion of massive plasmons is evaluated using the relation $\omega_p^2 = \frac{e^2}{4\varepsilon_0\varepsilon_r}\frac{n_M}{m^*}q_1$, where $\varepsilon_r \sim 6.3$ is the average permittivity of the materials surrounding the flake (silica/silicon substrate and air), e is the electron charge, ε_0 is the vacuum permittivity, n_M is the carrier density associated with the 2DEG and m_{eff}=0.15 m_0 is the effective mass of Bi_2Se_3, with m_0 electron mass. Good agreement with the data is obtained considering a surface carrier density $n_M = 6\cdot10^{10}$ cm^{-2}, which indicates charge-carrier depletion at the surface, in agreement with previous studies of Bi_2Se_3.

The comparison with the theoretical curve predicted in the case of propagating bulk plasmons or Dirac plasmons cannot fit the observed oscillations in $Bi_2Te_{2.2}Se_{0.8}$. To shed further light on the nature of these modes we then perform numerical simulations of the collective mode energy dispersion in our $Bi_2Te_{2.2}Se_{0.8}$ flakes. We look for the dispersion of phonon-polariton modes in the presence of charge carriers populating the TSS, described by the surface sheet conductivity of Dirac fermions, assuming that the chemical potential is located in the bulk band gap, resulting in a negligible bulk conductance. The charge-carriers in the TSS are expected to form Dirac plasmons that hybridize with the phonon-polariton modes to form hyperbolic plasmon-phonon-polaritons.

The near-field signal can be considered as a weighted average of the surface reflectivity for p- (or TM-) polarized light $r_P(q, \omega_0)$ over q. The dispersion of collective modes is identified by the maxima at real arguments q and ω of the imaginary part of the $r_P(q,\omega)$, which we calculate including the strong anisotropy of the frequency-dependent dielectric permittivity of $Bi_2Te_{2.2}Se_{0.8}$

The false color maps of the function $Im[r_P(q,\omega)]$ in Fig. 7 provide a convenient visualization of the collective mode spectra.

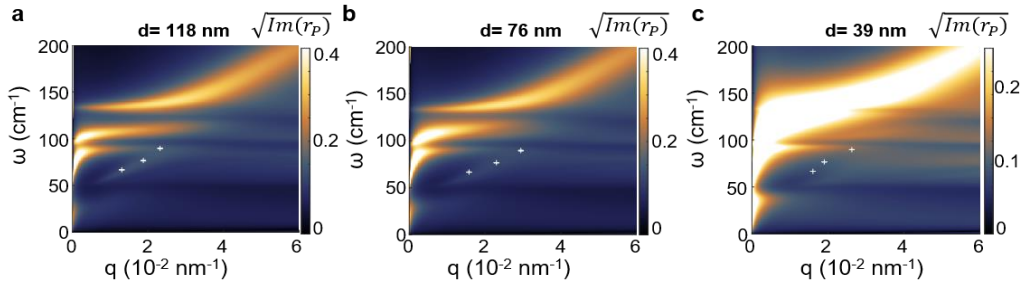

Figure 7: (a-c) Collective mode dispersions of Bi_2Te_3 slabs of different thickness, rendered using the false color maps of Im r_p. The parameters of the calculation are μ = 0.2 eV and (a) d = 118 nm; (b) d = 76 nm; (c) d = 39 nm. In the plots, the Fermi velocity is v_F = $0.5 \cdot 10^8$ cm/s as for Bi_2Te_3 from Ref.50, the electron scattering rate is γ_e =1 THz as in Ref.4, the vacuum and substrate permittivity are $\varepsilon_0 = 1$, and $\varepsilon_{sub} = 6.3$. The white symbols correspond to the experimental data of Fig. 5d.

The bright lines in Figs.7a-7c are the dispersion curves of the collective modes calculated for $Bi_2Te_{2.2}Se_{0.8}$ flakes of different thickness, assuming a constant chemical potential μ= 200 meV which is chosen to fall within the electronic bandgap of the material (~280meV). The Im{r_p} map calculated for chemical potentials μ= 50 meV, μ= 150 meV and μ=250 meV and for flake thickness 118 nm is reported in the Supplementary Information, Fig.S14. In bismuth chalcogenide compounds, the electrochemical potential is indeed expected to approach the bottom of the conduction band as a consequence of the doping due to vacancies or antisite defects. The smearing of the dispersion lines gives an idea of how damped the modes are. The comparison with our experimental data (white crosses in Figs. 7a-c), show that our photoexcited modes all fall in the upper half of the hyperbolic band $\omega_{to}^{\perp} < \omega < \omega_{to}^{//}$ and their q values correspond to those expected for hybrid modes resulting from hybridization of hyperbolic phonon-polaritons with TSS Dirac plasmons into combined hyperbolic plasmon-phonon-polaritons modes (HP^3 modes), and differ significantly from those expected when only Dirac plasmons come into play.
The hybridization of phonon-polariton with Dirac plasmon introduces additional control knobs, namely flake thickness and doping, to tune the HP^3 mode dispersion and accordingly the THz response of $Bi_2Te_{2.2}Se_{0.8}$ flakes. Moreover, since HP^3 modes are highly directional, a change in the doping can be exploited to vary the propagation direction of the HP^3.

Associated publications

EAA Pogna, L Viti, A Politano, M Brambilla, G Scamarcio, MS Vitiello *Mapping propagation of collective modes in Bi_2Se_3 and $Bi_2Te_{2.2}Se_{0.8}$ topological insulators by near-field terahertz nanoscopy* ***Nature communications*** 12 (1), 6672 (2021).

3. Fast and Sensitive Terahertz Detection Using an Antenna-Integrated Graphene pn Junction

Although the detection of light at terahertz (THz) frequencies is important for a large range of applications in the fields of medicine, security, quality testing, chemical spectroscopy, and more, current detectors typically have several disadvantages in terms of sensitivity, speed, operating temperature, and spectral range.

We designed and developed a novel detector for terahertz radiation that exploits the ability of graphene to efficiently convert absorbed light (of any wavelength) into hot graphene electrons. These hot electrons are subsequently responsible for creating a photoresponse through the thermoelectric effect.

Our novel, antenna-integrated THz photodetector design, is based on high mobility, hexagonal BN (hBN)-encapsulated graphene, with a device geometry that is explicitly designed towards exploiting the PTE effect. Specifically, we employed a dual-gated, dipolar antenna to simultaneously create a pn-junction in a graphene channel located above the antenna, and concentrated the incoming radiation at this pn-junction, where the photoresponse is created.

The detector contains a dipole antenna that is located 15 nm below the graphene channel. The antenna consists of two branches that are separated by a very narrow gap, with a size on the order of 100 nm. This antenna gap serves to focus the incoming THz radiation into a very small spot in the graphene channel. Here, the concentrated field of the antenna leads to (intraband) absorption and the subsequent creation of hot carriers. Since the creation of a photoresponse from hot carriers requires a gradient in the Seebeck coefficient, we use the antenna branches simultaneously as split gates. We apply appropriate voltages (V_L and V_R) to the left and right antenna branch, and through capacitive coupling this creates a pn-junction in the graphene channel, and thereby a THz-induced photoresponse. Thus, the antenna simultaneously creates the photo-active area in the graphene channel (located around the pn-junction, see Fig. 3c) and funnels incident radiation to this photo-active area, due to the very strong field enhancement of incident THz radiation above the gap between the two antenna branches (see Fig. 3a-b). Compared to previous antenna-integrated, graphene-based THz detectors, the advantage of our design is that the antenna gap is much smaller (100 nm vs: several microns), which means that the THz intensity is greatly enhanced (four orders of magnitude, see Fig. 3a). Also, there is no direct electrical connection between the antenna and the graphene, which means that there is no need for impedance matching to assure current flow between antenna and graphene.

Furthermore, we use hBN-encapsulated graphene, which leads to graphene with high mobility and low residual doping. This means that the resistance of the graphene channel will be low, and we can tune the system relatively close to the Dirac point (point of lowest carrier density), where the Seebeck coefficient is largest. Finally, we pattern the graphene channel into an "H-shape" with a relatively narrow (micron-sized) width. The narrow width of the central part of the channel leads to an enhanced photoresponse, as the hot carriers will have a higher temperature. The wider sides of the graphene channel reduce overall device resistance by minimizing contact resistance.

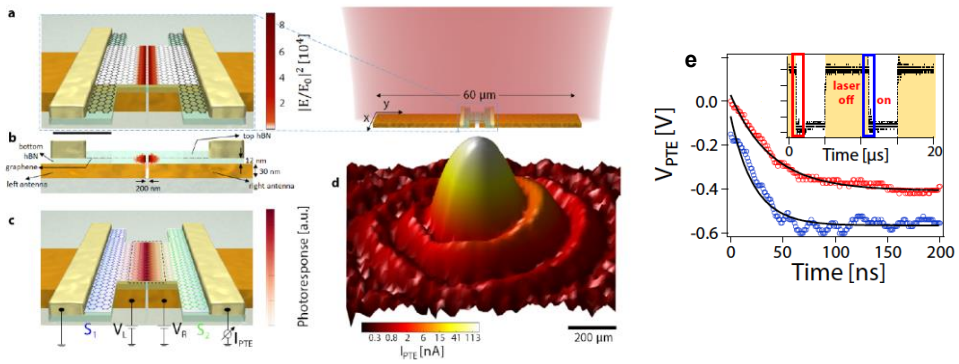

Figure 3. a) Schematic representation (right; not to scale) of the antenna-integrated pn-junction device and a zoom of the central part of the THz PTE detector (left; to scale). The color map superimposed on the device shows the simulated power profile at a position 5 nm below the graphene channel. The black scale bar corresponds to 1.6 µm. b) Side view of the device design, c) Same as panel a, now indicating how the antenna branches serve as local gates by applying voltages V_L and V_R. The color map superimposed on the device is a simulation that shows the photoresponse created by local photoexcitation d) Photocurrent image (log-scale) obtained by scanning the detector in the focal plane of a focused laser beam at 3.4 THz.
e) Results of the pulsed laser experiment, where the photocurrent was amplied by a fast current pre-amplifer and the data were acquired with a fast oscilloscope. The inset shows how the photovoltage V_{PTE} follows the switching of the pulsed laser. The red and blue (plotted with an oset) open dots show the obtained photovoltage in a small time window marked in the inset, with the black line giving the result of exponential fits with timescales of 40 (24) ns for the red (blue) curve.

We demonstrate that this novel detector has excellent sensitivity, with a noise-equivalent power of 80 pW/Hz$^{1/2}$ at room temperature, a response time below 30 ns (setup-limited), a high dynamic range (linear power dependence over more than 3 orders of magnitude), and broadband operation (measured range 1.8-4.2 THz, antenna-limited), with the potential of being extended to significantly lower and higher frequencies using appropriate antennas). Importantly, this detector simultaneously fulfills the requirements of room-temperature operation above 1 THz with short response time and 10 pW/Hz$^{1/2}$-order noise-equivalent power, a combination that is currently missing in the state of the art.

In addition, it has the advantage of being based on low-cost materials with scalable integration capabilities with the well-established CMOS electronics for low-cost imaging systems.34 Furthermore it is very low in power consumption, as it is a passive device.

Associated publications

S. Castilla, B. Terres, M. Autore, L. Viti, Jian Li, A. Nikitin, I. Vangelidis, K. Watanabe, T. Taniguchi, El. Lidorikis, M. S. Vitiello, R. Hillenbrand, K. Tielrooij, F. H.L. Koppens, *"Fast and sensitive terahertz detection using an antenna-integrated graphene pn-junction"* ***Nano Letters*** 2019, 19, 5, 2765–2773

4. Ultrafast two-dimensional field spectroscopy of terahertz intersubband saturable absorbers

Intersubband (ISB) transitions in semiconductor multi-quantum well (MQW) structures are promising candidates for the development of saturable absorbers at terahertz (THz) frequencies. We recently exploited amplitude and phase-resolved two-dimensional (2D) THz spectroscopy on the sub-cycle time scale to observe directly the saturation dynamics and coherent control of ISB transitions in a metal-insulator MQW structure. Clear signatures of incoherent pump-probe and coherent four-wave mixing signals are recorded as a function of the peak electric field of the single-cycle THz pulses. All nonlinear signals reach a pronounced maximum for a THz electric field amplitude of 11 kV/cm and decrease for higher fields. We demonstrate that this behavior is a fingerprint of THz-driven carrier-wave Rabi flopping. A numerical solution of the Maxwell-Bloch equations reproduces our experimental findings quantitatively and traces the trajectory of the Bloch vector. This microscopic model allows us to design tailored MQW structures with optimized dynamical properties for saturable absorbers that could be used in future compact semiconductor-based single-cycle THz sources.

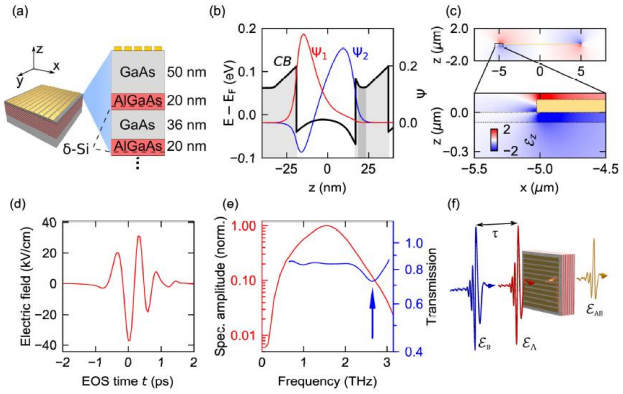

Figure 5. (a) Schematic diagram of the THz saturable absorber structure showing the grating and the MQW stack. δ-Si: Silicon delta-doping layers. (b) Electron envelope functions of the first and second subbands, and the conduction band edge (CB, black), in the MQW structure. (c) Cross section of the sample, showing the simulated field enhancement of the z-component Ez at 2.7 THz underneath one period of the gold grating, normalized to the incident electric field. Dashed horizontal lines indicate a GaAs layer, separating the MQW section from the metal grating.
Lower panel: magnified view of the marked part of the upper panel. (d) Electric field waveform of the THz pulses used to excite the ISB system. (e) Amplitude spectrum of the THz transient shown in (d) along with the measured field transmission of the sample. The blue arrow indicates the expected ISB transition frequency. (f) Experimental principle showing the two identical THz pulses with fields EA and EB delayed by a time τ , which prepare and interrogate the structure's nonlinear response.

Associated publications

J Raab, C Lange, JL Boland, I Laepple, M Furthmeier, E Dardanis, N. Desmann, L. Li, G.A. Davies, E.H. Linfield, M.S. Vitiello and R. Huber "*Ultrafast two-dimensional field spectroscopy of terahertz intersubband saturable absorbers*" ***Optics Express*** 27, pp. 2248-2257 (2019).

Project 2: Quantum Effects in Complex Systems ('Q-EX')

Institution: Princeton University, Princeton, NJ; Polytechnic University of Milan Supervisor: Federico Capasso
Proposed beneficiary: Dr. Margherita Maiuri **(**Chemistry, Princeton University, and Physics, Polytechnic University of Milan)

1. Ultrafast dynamics in bio-inspired molecular arrays

Organic small molecules, such as tetrapyrroles, play crucial roles in numerous processes in nature, serving as cofactors in proteins where they have several functions. For example, chlorophylls (which contain magnesium ions) are responsible for photosynthetic electron and energy transfer, whereas hemes (which are iron porphyrins) contribute to the transport of diatomic gases.

In the last two decades, a huge range of conjugated porphyrin arrays have been investigated, with the goal of synthetizing efficient bioinspired molecular systems for light harvesting, charge separation, or photocatalytic processes. Characterizing the photoinduced ultrafast processes involved in these molecules is necessary for understanding such processes.

This project exploits a series of zinc-porphyrin arrays recently synthesized, noncovalently linked through benzene-based hubs, with the aim of mimicking the structure and function of some chromophores in photosynthetic reaction centers. Compared to previous porphyrin arrays, the flexibility of the central hub allows the monomers to interact with each other via face-to-face π–π-stacking without any direct conjugation, making such systems excellent models for studying excitonic interactions in natural complexes such as those in bacterio-chloprohylls special pairs. Excitonic coupling of the porphyrin subunits is expected to activate additional excited state relaxation channels with respect to the monomer, which have not been observed so far.

The appearance of such supramolecular electronic interactions has been revealed, using ultrafast transient absorption spectroscopy with sub-25 fs time resolution. Upon photoexcitation of the Soret band, energy trapping within ~150 fs is resolved in a delocalized dark excitonic manifold. Moreover, excitonic interactions promote an additional fast internal conversion from the Q-band to the ground state with an efficiency of up to 60% in the hexamer. These relaxation pathways appear to be common loss channels that limit the lifetime of the exciton states in noncovalently bound molecular aggregates.

Associated Publications

L. Moretti, B. Kudisch, Y. Terazono, A. Moore, T. A. Moore, D. Gust, G. Cerullo, G.

D. Scholes, M. Maiuri. "Ultrafast Dynamics of Nonrigid Zinc-Porphyrin Arrays Mimicking the Photosynthetic 'Special Pair'." 11, 3443-3450, *J. Phys. Chem Lett*. (2020).

2. Excitonic interactions in 2D materials and their heterostructures

Atomically thin transition-metal dichalcogenides (TMDs) have come into the spotlight in optoelectronics thanks to their outstanding physical properties. Because of the strong quantum confinement effects, Coulomb interaction is poorly screened in single-layer (1L) TMDs, so that the excitons created by photo-excitation have large binding energy, up to several hundred meVs.

Among TMDs, MoS_2 has emerged as a promising candidate for the semiconducting analogue of graphene. While the steady-state properties of TMDs have been studied in detail by linear optical techniques, the recent application of time-resolved nonlinear spectroscopy has enabled the study of excited-state dynamics on femtosecond timescales, mainly employing ultrafast pump-probe spectroscopy. Although exciton dynamics in few- and monolayer TMDs have been largely studied in the past years, a

complete understanding of the mechanisms leading to ultrafast exciton formation and couplings is far from being understood.

This project exploits ultrafast two-dimensional electronic spectroscopy (2DES) to unveil exciton dynamics in monolayer MoS_2. 2DES provides a more comprehensive picture of the excitonic response compared to pump-probe, since it gives simultaneous spectral and temporal resolution on the excitation and detection axes. By using a sequence of 3 pulses, 2DES improves over two-pulse pump-probe spectroscopy in its ability to map the full third-order optical susceptibility of a sample by correlating excitation and detection frequencies. Through this approach several physical insights have been achieved: direct measurements of the homogeneous/inhomogeneous broadenings, strong coherent interaction between excitons and trions, and signatures of biexcitons. Here the team reports broadband 2DES measurements on monolayer Mos_2 at 77K and room temperature, using sub 20-fs broadband pulses resonant with both exciton transitions. The project's findings: (i) an ultrafast sub-50fs decay of the diagonal peaks due to optical exciton decoherence, dominated by inhomogeneous broadening and (ii) two cross-peaks relaxations feature, due to scattering towards dark exciton states, as predicted for $MoSe_2$ before.

A second follow-up project applied two-dimensional electronic spectroscopy (2DES) to study ultrafast processes in TMDs heterostructures (HS). In TMD-HS with type-II band alignment, interlayer charge transfer (ICT) occurs such that a hole and electron reside in different layers, resulting in an inter-layer exciton with a recombination lifetime at least an order of magnitude longer than intra-layer exciton recombination times. 2DES measurements of ICT in a WS_2/MoS_2 HS using sub-30 fs broadband pulses are presented. The team resolved hole-transfer from the MoS_2 layer on sub-20 fs timescales. Signatures of electron transfer are also present but are less well spectrally distinguished. Due to the broadband nature of this 2DES experiment the team additionally resolved dependence of the interlayer charge transfer rate on the energy difference between the electron or hole donating and accepting layers.

Associated publications

M. Maiuri, S. Dal Conte, M. Russo, J. Wang G. Soavi, D. Dumcenco, A. Kis, A.C. Ferrari, G. Cerullo. "Excitonic Effects in Single Layer MoS2 Probed by Broadband Two-dimensional Electronic Spectroscopy." 2019 Conference on Lasers and Electro-Optics *(CLEO)*, San Jose, CA, USA, 2019, pp.1-2.

V. R. Policht, M. Russo, F. Liu, C. Trovatello, M. Maiuri, S. Dal Conte, X. Zhu, G. Cerullo "Observation of Interlayer Charge Transfer in Transition Metal Dichalcogenide Heterostructures via Time-resolved Two-Dimensional Electronic Spectroscopy." Manuscript in preparation.

3. *Ultrafast broadband dichroism by transient optical symmetry breaking in plasmonic metasurfaces*

Ultrafast nanophotonics is an emerging research area aimed at the development of nanodevices capable of light modulation with unprecedented speed. A promising approach exploits the optical nonlinearity of nanostructured materials, metallic or dielectric, to modulate their effective permittivity via interaction with intense ultrashort optical pulses. A variety of configurations has been reported and the temporal dynamics following photoexcitation has been intensely investigated, both experimentally and theoretically. This is especially true for plasmonic nanostructures, where ultrashort optical pulses trigger a delayed third-order nonlinear response dictated by internal relaxation of the metallic nanosystems, allowing all-optical light modulation. While the ultrafast temporal dynamics following photoexcitation has been deeply investigated, subpicosecond spatial inhomogeneity occurring at the nanoscale has been so far neglected.

A current open challenge in manipulating ultrashort intense laser pulses remains the feasibility of all-optical modulation of light over a broad bandwidth, with a full recovery over an

ultrafast subpicosecond timescale. Among the different kinds of all- optical functionalities, ultrafast polarization switching has recently attracted a huge interest for advanced applications in photonics and beyond. In this work, the team combines polarization-resolved pump-probe spectroscopy with a quantitative numerical model able to describe the ultrafast nanoscale inhomogeneities at very early times upon photoexcitation.

The rationale of this project is the following: prediction and observation that photoinduced spatio-temporal transients can break the symmetry of a plasmonic metasurface even if composed of highly symmetric metaatoms, thus generating a broadband dichroic response with ultrafast recovery of the initial isotropic configuration well before the complete relaxation of the nanostructure.

A plasmonic metasurface made of a square array of closely packed C4 symmetric gold nanocrosses with thickness H = 45 nm, width W = 60 nm and length L = 165 nm is considered. Such a symmetric nanomaterial provides a polarization independent static transmittance at normal incidence characterized by a broad dip around 800 nm, due to the degenerate longitudinal plasmonic resonances of the two arms of the nanocross and broadened by hybridization effects in the array. Such a degeneracy can be broken by the resonant absorption of an ultrashort pump pulse with linear polarization parallel to the direction of one of the arms. Photo-absorption creates a highly inhomogeneous near field, mostly because of the retardation-based nature of plasmonic resonances in relatively large nanostructures. The inhomogeneous absorption pattern in each metaatom locally affects the electronic population of gold, inducing a non-uniform out of equilibrium hot-carriers distribution which anisotropically modifies the metal permittivity. The fingerprint of the ultrafast pump-induced symmetry breaking is a transient transmission anisotropy, which can be revealed in a polarization-resolved pump-probe experiment where the delayed probe pulse impinges at normal incidence with a linear polarization at 45 degrees to the nanocross arms.

A quantitative numerical model describes the ultrafast spatial transients in terms of three spatial and temporal variables specifying the internal energy dynamics in gold: the energy density stored in the non-thermal fraction of photoexcited carriers, the temperature of the thermalized population of hot electrons and the lattice temperature (which plays a minor role on the sub-picosecond time scales). These three variables are interlinked by a set of three coupled partial differential equations, referred to as the Inhomogeneous Three-Temperature Model (I3TM) which extends the popular 3TM, widely used so far for metallic and semiconducting nanostructures, by including the spatial dependence of the variables.

The team then employs finite-element method numerical analysis in the frequency domain to calculate the transmission spectrum of the metasurface at normal incidence for a linear polarization parallel and orthogonal to the pump, for a set of permittivity configurations obtained by sampling the gold permittivity distribution at different pump-probe delays. The difference of the relative differential transmittance for parallel and perpendicular probe polarizations results in a broadband ultrafast transient dichroism. The main contribution to the phenomenon arises from non-thermal carriers.

These theoretical predictions are compared with polarization resolved ultrafast pump- probe experiments. The metasurface is resonantly pumped by a 30-fs pulse at 850 nm and the relative differential transmittance is probed by a 10-fs visible pulse spanning the 565-735 nm wavelength range. A good agreement is retrieved both for the spectra and the dynamics of the pump-probe experiment.

This project has shown that photoexcitation of a plasmonic metasurface by an ultrashort optical pulse induces a transient symmetry breaking. Such spatio-temporal electronic transients at the nanoscale translate into an anisotropic local permittivity distribution, and subsequent ultrafast dichroic optical response of the metasurface, dominated by non-thermal hot-electrons dynamics. This modulation is broadband and returns to the isotropic configuration within few hundreds of fs. The project's results pave the way to all-optical control of light at Tera bit/s speed, with particular relevance for ultrafast polarization management.

Associated publications

A. Schirato*, M. Maiuri*, A. Toma, R. Proietti Zaccaria, P. Laporta, P. Nordlander, G. Cerullo, A. Alabastri, G. Della Valle. "Ultrafast Broadband Dichroism by Transient Optical Symmetry Breaking in Plasmonic Metasurfaces." Submitted to *Nature Photonics*.

4. Plasmonic nanoparticle assemblies for light-activated drug release probed with ultrafast spectroscopy

Novel regenerative strategies aim to design advanced therapies for patients with severe or chronic diseases where body's own response is not enough for the recovery of all functions. In the last years, researchers focused their attention on two strategies using biomaterials as carriers: i) stem cell-based technologies, ii) target/local delivery of specific drug and biomolecules (i.e., growth factors, cytokines). The major challenges of recent works are to improve drug loading, increase selectivity to target cells, and control the precise release of drugs.

This project focused on hydrogels, hydrophilic biocompatible three-dimensional networks, which found many applications in cartilage, central nervous system and bone repair strategies. Their mild gelling condition and elastic properties allow their use as carriers for drugs and cells at the same time. Indeed, by tuning their swelling properties, degradation rate and cross-linking density, it is possible to smartly control cell fate and release rates. However, the extremely good results obtained as cell carriers do not have the right corresponding in drug delivery applications both with hydrophobic and hydrophilic drugs. It is known that mechanisms involved in drug delivery through hydrogels are: i) Fickian diffusion, ii) swelling, and iii) degradation. This project aims to tune the swelling of the three-dimensional network in order to guarantee drug release only after a specific stimulus.

The team investigated the use of light irradiation of hydrogel networks to ameliorate the performances of a hydrogel library developed for cell-based therapies, obtained by synthesis from block polycondensation between agarose and carbomer, together with cross-linkers. To make such hydrogels light-responsive, gold-based nanoparticles (Au NPs) were physically entrapped within the hydrogel networks forming organic- inorganic composite materials. The ability of Au NPs to make organic networks sensible to light irradiation is well known in literature, and many research groups described the promising possibility to load Au NPs within polymeric network to improve cancer treatment, antimicrobial activity, or bone regeneration.

The hybrid sample was studied as drug delivery system with and without light irradiation, both from experimental and modelling perspectives, loading composite hydrogels with a specific drug (dextran 70 kDa conjugated with fluorescein) that may mimic high steric hindrance therapeutic molecules like a wide class of proteins, such as antibodies or erythropoietin. The role of NPs PEGylation was widely studied for NPs colloidal stability while its influence in light-responsive induced materials is unexplored.

This project's results indicate that the use (or not) of PEGylation onto Au NPs can dramatically tune the final performance of the drug delivery devices, posing questions about the aggregation condition of the NPs in the gel. To unveil the physical mechanisms triggering the different drug release trends, ultrafast pump-probe spectroscopy was performed on the two classes of NPs-loaded hydrogel without any drugs to relate their photo-physics with the performances of the drug-loaded vehicles. By combining the ultrafast experiment with modeling, the project suggests a higher heat transfer efficiency of NPs aggregates respect to the isolated NPs, which supports the results retrieved from the drug delivery study.

Associated publications

L. Moretti, A. Rossetti, A. Mazzanti, L. Polito, F. Pizzetti, G. Della Valle, G. Cerullo, A. Sacchetti, F. Rossi, M. Maiuri. "Plasmonic Nanoparticles Assemblies Control Light-Activated Drug Release." Manuscript in preparation.

5. Ultrafast spectroscopy: state of the art and open challenges

The project supported the realization of a perspective article on ultrafast spectroscopy.

Ultrafast spectroscopy techniques use sequences of ultrashort light pulses (with femto- to attosecond durations) to study photo-induced dynamical processes in atoms, molecules, nanostructures, and solids. This field of research has experienced an impetuous growth in recent years, due to the technological progress in the generation of ultrashort light pulses and to the development of sophisticated spectroscopic techniques, which greatly increase the amount of information on the process under study. This paper aims to provide a non-exhaustive overview of the state of the art of the field and point out future challenges. After first reviewing progress in ultrafast optics, which has enabled the generation of broadly tunable light pulses with duration down to a few optical cycles, the pump-probe technique is then discussed, showing examples of its capability to combine very high time resolution, down to the attosecond regime, with broad spectral coverage. Two-dimensional spectroscopy is introduced, and results that demonstrate the additional information content provided by the combination of temporal and spectral resolution are presented. After a review of the achievements of ultrafast X-ray and electron diffraction, which provide time- dependent structural information on photochemical processes, the article concludes with a critical analysis of the future open challenges in the field.

Associated publications

M. Maiuri, M. Garavelli, G. Cerullo. “Ultrafast Spectroscopy: State of the Art and Open Challenges” 142, 3-15 *Journal of the American Chemical Society* (2020).